JⱮ PAPERS

Manifestation of screech modes in non-axisymmetric jets

Soudeh Mazharmanesh[1,†], **Petrônio A.S. Nogueira**[1], **Joel Weightman**[1] **and Daniel Edgington-Mitchell**[1]

[1]Department of Mechanical and Aerospace Engineering, Monash University, Melbourne, VIC 3800, Australia

This study identifies two previously unrecognised screech modes in non-axisymmetric jets. Spectral proper orthogonal decomposition (SPOD) of ultra-high-speed schlieren images reveals a bi-axial flapping mode in a rectangular jet and a quasi-helical mode in an elliptical jet. To educe the complex three-dimensional structure of these new modes, SPOD is performed on datasets from different viewing perspectives, produced by rotating the nozzle with respect to the schlieren path to an azimuthal angle θ. The bi-axial flapping mode is strongly antisymmetric from any perspective. However, the SPOD eigenvalue at the screech frequency (λ_s) varies with θ and the axial distance of the SPOD domain from the nozzle lip. This mode most closely resembles a flapping mode in the minor-axis plane close to the nozzle lip and a wagging mode in the major-axis plane further downstream. This transition from flapping to wagging at the same frequency correlates with the axis switching defined by the shock-cell structure in the mean flow. The quasi-helical mode in the elliptical jet is characterised by an antisymmetric structure present in the SPOD spatial modes whose eigenvalue λ_s is insensitive to both θ and the axial domain. These findings indicate that the spatial evolution of the mean flow in non-axisymmetric jets may allow them to support a range of additional screech modes that differ significantly from those supported by the original three-dimensional shape of the jet.

Key words: jet noise, shock waves, jets

1. Introduction

Increasingly stringent regulations on jet noise are motivated both by population growth leading to airports in closer proximity to population centres and by an expanding body of evidence linking exposure to jet noise to poor health outcomes. The sound produced by

† Email address for correspondence: soudeh.mazharmanesh@monash.edu

the turbulent jet emitted from gas-turbine engine exhausts remains the major contributor to overall noise during takeoff, despite significant strides in reducing this noise component through a reduction in exhaust velocities. Aircraft designed to fly above the speed of sound, whether military jets or supersonic civilian-transport concepts, cannot achieve reductions via the same means. The exhaust from these engines, even at takeoff, is supersonic and likely to contain shock and expansion waves, which motivates further attempts to understand, and ultimately control, the noise produced by imperfectly expanded supersonic jets (Tam 1995). These jets are characterised by a range of noise sources, both broadband and tonal. Like subsonic jets, the dominant noise source in the downstream direction remains that associated with the turbulent wavepackets (Cavalieri *et al.* 2013; Jordan & Colonius 2013; Cavalieri, Jordan & Lesshafft 2019). The presence of shocks, as well as modifying these wavepackets (Nogueira *et al.* 2022*c*), introduces new sources of sound, including broadband shock-associated noise (Harper-Bourne & Fisher 1974) and screech (Edgington-Mitchell 2019). Though the aforementioned sources are observed in jets at all scales, jets at full scale also exhibit noise sources which have no clear counterpart in the laboratory (Leete *et al.* 2021). Of these various sound sources, the focus of this paper is on unusual manifestations of jet screech in non-axisymmetric jets.

The occurrence of jet screech was initially discovered by Powell (1953), who proposed that it was due to a resonance loop. According to the classical explanation of jet screech, the instability waves in the jet shear layer propagate downstream and interact with shock structures. This interaction leads to the creation of waves propagating upstream. These upstream-travelling waves then propagate back to the nozzle, disturbing the shear layer and initiating new instability waves, thus completing the resonance loop (Tam & Tanna 1982). The wave travelling downstream has long been recognised as the Kelvin–Helmholtz (KH) wavepacket (Cavalieri *et al.* 2013), while the wave travelling upstream has recently been identified as a subsonic guided jet mode (G-JM), first predicted by Tam & Hu (1989), and identified in subsonic impinging (Tam & Ahuja 1990) and free (Schmidt *et al.* 2017; Towne *et al.* 2017) jets in subsequent decades. This mode has since also been identified in supersonic impinging (Bogey & Gojon 2017), then screeching (Edgington-Mitchell *et al.* 2018; Gojon, Bogey & Mihaescu 2018) and finally ideally expanded (Bogey 2021) jets. The general mechanism behind screech is now well understood, as detailed by Nogueira *et al.* (2022*b*) and Edgington-Mitchell *et al.* (2022*a*), being an extension of the 'weakest-link' model of Tam & Tanna (1982) that considers the upstream wave as a guided jet mode and accounts for variation in shock-cell spacing (Nogueira *et al.* 2022*a*). The core of the weakest-link model is that the wavenumber of the upstream-propagating wave is selected via a triadic interaction between the Kelvin–Helmholtz (KH) wavepackets and the shock structures.

Modal-staging behaviour in axisymmetric jets has been investigated systematically in prior research (Powell 1953; Davies & Oldfield 1962; Powell, Umeda & Ishii 1992; Singh & Chatterjee 2007; Gao & Li 2010; Edgington-Mitchell *et al.* 2022*a*). It has been shown that the discrete jump in frequency often (but not always) coincides with a modification in the azimuthal structure of the screech mode. Screech modes have historically been denoted classified according to their azimuthal structure, toroidal (A1 and A2), flapping (B and D) and helical (C) disturbances. These modes can be linked to the natural instability of the jet, which can be decomposed on an azimuthal basis into modes categorised by their azimuthal wavenumber, denoted m. Additionally, A1 and A2 have been found to be linked to the $m = 0$ mode. The helical C mode is associated with the $m = \pm 1$ mode. The B and D flapping modes are considered a special case of the $m = \pm 1$ modes, where two helical

modes happen simultaneously with a consistent phase relationship, resulting in a flapping mode.

Early studies on jet screech have focused on axisymmetric jets. Later, researchers found that alternative non-axisymmetric nozzle geometries such as rectangular and elliptical shapes notably enhance noise suppression (Wlezien & Kibens 1988; Viswanath *et al.* 2017) and large-scale turbulent mixing (Ho & Gutmark 1987; Gutmark, Schadow & Wilson 1989; Gutmark & Grinstein 1999). Motivated by these benefits, supersonic jets issuing from an elliptical nozzle have been studied theoretically using stability analysis (Crighton 1973; Morris 1988; Morris & Bhat 1995; Kinzie & McLaughlin 1997; Morris 2010; Nogueira, Weightman & Edgington-Mitchell 2023) and experimentally (Ho & Gutmark 1987; Hussain & Husain 1989; Lee & Baek 1994; Rajakuperan & Ramaswamy 1998; Gutmark & Grinstein 1999; Yoon & Lee 2003; Edgington-Mitchell, Honnery & Soria 2015*a*,*b*). Two dominant screech modes have been observed in experimental studies, namely the varicose and flapping modes. Overall, five classes of instability waves have been predicted by linearised spatial stability analysis in the context of elliptical jets (Morris 1988; Morris & Bhat 1995; Nogueira *et al.* 2023; Suzuki, Nogueira & Edgington-Mitchell 2023). They are the varicose (ce_0), flapping (se_1), wagging (ce_1), double-flapping diagonally (ce_2) and double-flapping sidewards (se_2) modes. The ce_0 corresponds to the toroidal $m = 0$ mode in the axisymmetric jet case, becoming identical in the limit as the aspect ratio approaches 1. The se_1 and ce_1 are likewise equivalent to the $|m| = 1$ modes in the limit of AR $= 1$, but more closely resemble the flapping B and D screech modes away from this limit. In an axisymmetric jet, there is no preferred axis for the flapping mode, and it tends to precess around the axis. In an elliptical jet, the se_1 and ce_1 modes are locked to their particular axes.

Edgington-Mitchell *et al.* (2015*b*) observed a screech mode that appeared to be helical in nature, based on velocity measurements in two planes for an elliptical jet. The occurrence of this mode was explained through axis switching. Axis switching is a phenomenon specific to non-axisymmetric jets, in which the major axis of the jet contracts while the minor axis expands (Hussain & Husain 1989). This contraction and expansion leads to a switching of the axes, such that at some distance downstream of the nozzle, the jet has greater spanwise extent in what was originally the minor axis. Edgington-Mitchell *et al.* (2015*b*) hypothesised that the deformation of the mean flow in the form of axis switching might permit the flow to support more modes than stability analysis of an elliptical profile might suggest. However, this was speculation, and no further evidence of this 'helical' mode has appeared in the literature.

Some experimental (Suda, Manning & Kaji 1993; Raman & Rice 1994; Raman 1997; Menon & Skews 2010; Karnam, Baier & Gutmark 2019; Semlitsch *et al.* 2020; Edgington-Mitchell, Beekman & Nogueira 2022*b*; Karnam, Saleem & Gutmark 2023) and numerical (Umeda *et al.* 1990; Cain *et al.* 1995; Berland, Bogey & Bailly 2007; Viswanath *et al.* 2017; Chakrabarti, Gaitonde & Unnikrishnan 2021; Liang *et al.* 2023) studies have been also conducted on rectangular jets. Overall, the flapping mode in the minor-axis plane and the varicose mode have been found to dominate the screeching behaviour of rectangular jets. Raman (1997) briefly reported the existence of antisymmetric screech modes in the major-axis plane for a rectangular jet with aspect ratio AR $=$ 5.0. Our experimental results indicated that rectangular and elliptical jets can produce an antisymmetric screech mode in the major-axis plane (Mazharmanesh *et al.* 2024). However, characterisation of this mode has remained underexplored.

This study is motivated by these preliminary data that suggest the presence of additional heretofore undocumented antisymmetric screech modes in non-axisymmetric jets. In this
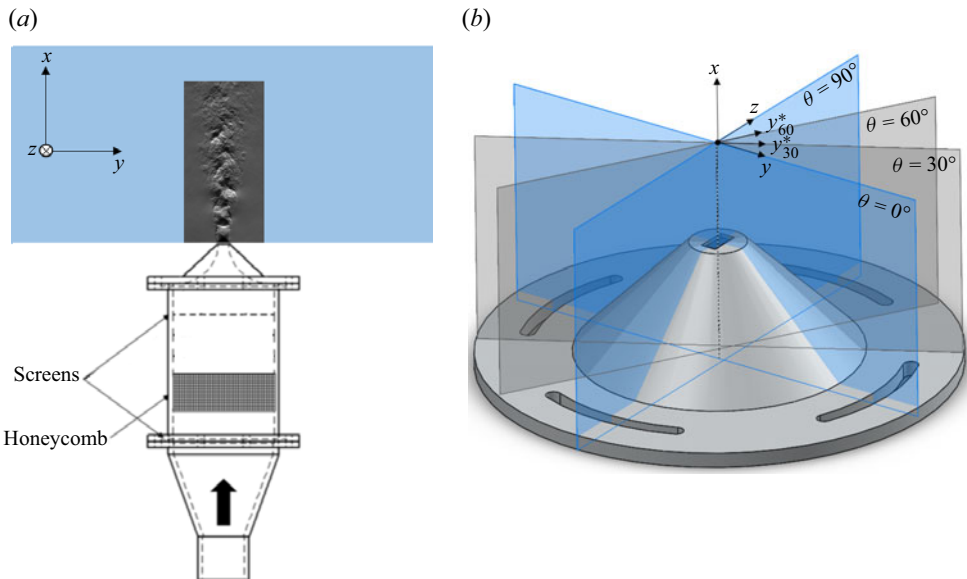
(*a*)

(*b*)

Figure 1. (*a*) Schematic of the supersonic-jet experimental facility. (*b*) Rectangular-nozzle geometry and global coordinate system. Minor-axis and major-axis planes are marked by $\theta = 0°$ and $\theta = 90°$, respectively.

paper, we systematically characterise all the screech modes observed in rectangular and elliptical jets, including two new observed modes we label as 'Bi-axial flapping' and 'Quasi-helical' modes. High-speed schlieren visualisations accompanied by spectral proper orthogonal decomposition (SPOD) are used to classify the screech modes. This paper is organised as follows. The experimental set-up and analysis techniques are described in § 2. Overall characteristics of the previously identified screech modes, i.e. varicose and flapping modes, are presented in § 3. Section 4 describes features of the new bi-axial flapping mode in rectangular jets, while characteristics of the quasi-helical mode observed in elliptical jet are discussed in § 5. The paper is completed with conclusions in § 6.

2. Experimental set-up

2.1. *Jet and nozzle parameters*

The experiments were performed in the Supersonic-Gas-Jet Facility at Monash University. A schematic of the supersonic-jet set-up is shown in figure 1(*a*). The system is supplied with a continuous flow of high-pressure air at nozzle pressure ratios NPR = 2.0–5.0, where NPR is the ratio of the plenum to the ambient pressure. Flow conditioning is achieved before entering the nozzle by using a series of screens and honeycombs in the plenum chamber. Two different nozzles are used in this study. The first nozzle is a purely convergent rectangular nozzle with an aspect ratio AR = 2.0, equivalent circular diameter $D_e = 13.6$ mm, and a non-uniform lip thickness between the major and minor axes due to uniform external geometry, as shown in figure 1(*b*). The other nozzle is a purely convergent elliptical nozzle with an aspect ratio AR = 2.0, equivalent circular diameter $D_e = 10$ mm and lip thickness $0.05D_e$. Both nozzles have a large contraction between plenum and throat of more than 100:1.

1004 A7-4

2.2. *Data acquisition*

The supersonic jet is visualised using a Z-type Toepler schlieren system consisting of two mirrors with focal length 2032 mm to create a collimated light path through the test section. Images are captured via a high-speed camera (Photron Fastcam SA-Z 2100k) operating at 150k frames per second with a shutter speed of 1/197647 s and resolution 512×200 pixels. Illumination is produced by a pulsed light-emitting diode (Willert *et al.* 2010) to obtain 100k images of density gradient in the streamwise direction ($\partial \rho / \partial x$) at each operating condition. In this study, schlieren measurements are taken from different azimuthal angles to reconstruct three-dimensional (3-D) flow structures of the supersonic jet. The camera is initially aligned with the minor-axis plane as marked by $\theta = 0°$ in figure 1(*b*) and the jet is displayed in the *x*–*y* plane. To capture different viewing perspectives, the nozzle is rotated about the *x*-axis from $\theta = 0°$ to $\theta = 180°$ in $10°$ increments while the camera position is kept constant. The co-ordinate y^* is used to denote the spanwise direction as defined by the viewing angle, while *y* and *z* are based on the nozzle geometry and are independent of viewing angle, as shown in figure 1(*b*). Here, $y^* = y$ when $\theta = 0°$ and $y^* = z$ when $\theta = 90°$.

2.3. *Data decomposition*

Spectral proper orthogonal decomposition (SPOD) (Lumley 1970; Towne, Schmidt & Colonius 2018) is a frequency-domain adaptation of the POD (proper orthogonal decomposition) technique. It identifies the most-energetic structures for specific frequencies. It is now well established as a methodology for identifying coherent structures for specific frequencies in turbulent flows (Schmidt *et al.* 2018; Sano *et al.* 2019; Abreu *et al.* 2021). SPOD identifies monochromatic modes that are optimal in terms of the flow's energy norm. The SPOD modes are derived as the eigenvectors of the cross-spectral density matrix, which is estimated using Welch's method (Welch 1967). A brief overview of the method is provided here, while comprehensive mathematical derivations and algorithmic details can be found from Towne *et al.* (2018) and Schmidt & Colonius (2020).

In statistically stationary flows, consider $q_i = q(t_i)$ as the mean-subtracted snapshots, where $i = 1, 2, \ldots, n_t$ indexes the number of snapshots. For spectral estimation, the dataset is segmented into n_{blk} overlapping blocks, each containing n_{fft} snapshots. Adjacent blocks overlap by n_{ovlp} snapshots, with $n_{ovlp} = n_{fft}/2$ for the present case (50 % overlap). Each of the n_{blk} blocks undergoes a Fourier transform in time, and all Fourier realisations at the *l*th frequency, denoted as $q_l^{(j)}$, are organised into a matrix $\widehat{Q}_l = [\hat{q}_l^{(1)}, \hat{q}_l^{(2)}, \ldots, \hat{q}_l^{(n_{blk})}]$. The SPOD eigenvalues Λ_l are determined by solving the eigenvalue problem $(1/n_{blk})\hat{Q}_l^* W \hat{Q}_l \Psi_l = \Psi_l \Lambda_l$, where W is a positive-definite Hermitian matrix accounting for the component-wise and numerical quadrature weights, and $(\cdot)^*$ indicates the complex conjugate. The SPOD modes for the *l*th frequency are then obtained as $\Phi_l = (1/\sqrt{n_{blk}})\hat{Q}_l \Psi_l \Lambda_l^{-1/2}$. The eigenvalues $\Lambda_l = \mathrm{diag}(\lambda_l^{(1)}, \lambda_l^{(2)}, \ldots, \lambda_l^{(n_{blk})})$ represent the energies of the corresponding SPOD modes, with $\lambda_l^{(1)} \geq \lambda_l^{(2)} \geq \cdots \geq \lambda_l^{(n_{blk})}$. The SPOD modes, denoted by the columns of the matrix $\Phi_l = [\phi_l^{(1)}, \phi_l^{(2)}, \ldots, \phi_l^{(n_{blk})}]$, represent the coherent structures in the flow at the *l*th frequency, with $\phi_l^{(j)}$ being the *j*th mode.

The SPOD will be used in this study to characterise the screech modes; flows characterised by resonance tend to exhibit low-rank behaviour and are thus amenable to decompositions of this kind (Wong *et al.* 2023). Here, we apply SPOD on the
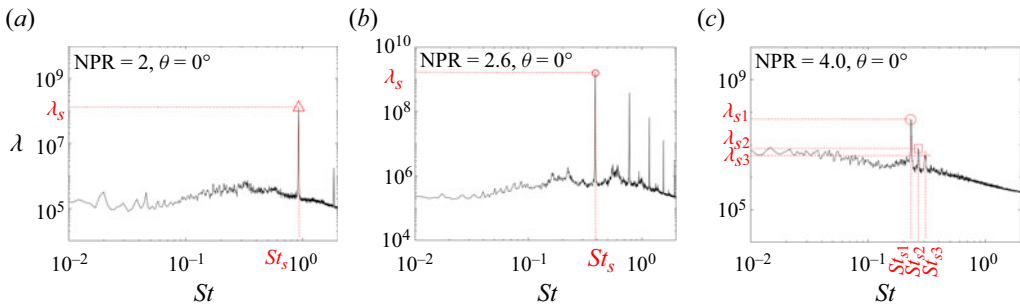
Figure 2. The SPOD-eigenvalue spectra of the leading mode for the rectangular jet viewed in the minor-axis plane ($\theta = 0°$) at: (*a*) NPR = 2.0; (*b*) NPR = 2.6; (*c*) NPR = 4.0. St_s and λ_s indicate the screech frequency and associated SPOD eigenvalue, respectively.

light-intensity data derived from schlieren to educe spatial modes ϕ and corresponding SPOD eigenvalues λ at the screech frequencies. It is noteworthy that the magnitude of the SPOD eigenvalues can only be used here for a qualitative comparison between cases; the magnitudes themselves are related to the degree of light-intensity fluctuation, rather than any fundamental flow variable. Sensitivity tests have been conducted by doubling the sample length to ascertain the influence of temporal period on the convergence for the leading SPOD modes. Further details of the statistical convergence of SPOD can be found in Appendix A. The spectral-estimation parameters used here are $n_{fft} = 4096$ and $n_{ovlp} = 2048$, resulting in $n_{blk} = 47$ SPOD modes for each frequency. The dataset used herein has $n_t = 100\,000$ snapshots.

3. Overall characteristics of the varicose and flapping modes

We begin with an analysis of the well-known varicose and flapping modes in both elliptical and rectangular jets. The SPOD eigenvalues are used to identify the frequencies associated with screech. Figure 2 shows exemplar SPOD-eigenvalue spectra of the leading mode for the rectangular jet at three different NPRs, as visualised in the minor-axis plane; the fundamental screech frequencies are denoted by red markers. In this study, the non-dimensionalised frequency, Strouhal number, is defined as $St = f D_e/U_j$, where D_e and U_j are the equivalent diameters (based on matched area) and ideally expanded jet exit velocities, respectively. Here, St_s and λ_s indicate screech frequency and associated SPOD eigenvalue, respectively. For the two lower NPRs presented, all the significant peak frequencies are harmonics of St_s, suggesting that only one screech loop is active (see figure 2*a*,*b*). As NPR increases, multiple non-harmonic peak frequencies appear in SPOD energy spectra, indicating multimodal behaviour (Edgington-Mitchell *et al.* 2022*a*), which means that more than one screech loop is active at a single operating condition (see figure 2*c*).

The SPOD-eigenvalue spectra for both jets and all NPR considered are presented as a contour in figure 3. In this figure, each spectrum at each NPR is individually normalised using its own maximum such that at each condition, the range of values is between 0 and 1. Peaks identified as per figure 2 are overlaid here using cyan markers. Only the initial and final pressures at which these peaks appear in the SPOD-eigenvalue spectra have been highlighted by the cyan markers in figure 3. Figure 3 demonstrates that multimodal behaviour occurs for both rectangular and elliptical jets at multiple operating conditions. It is noteworthy that multimodality is evident in both minor-axis
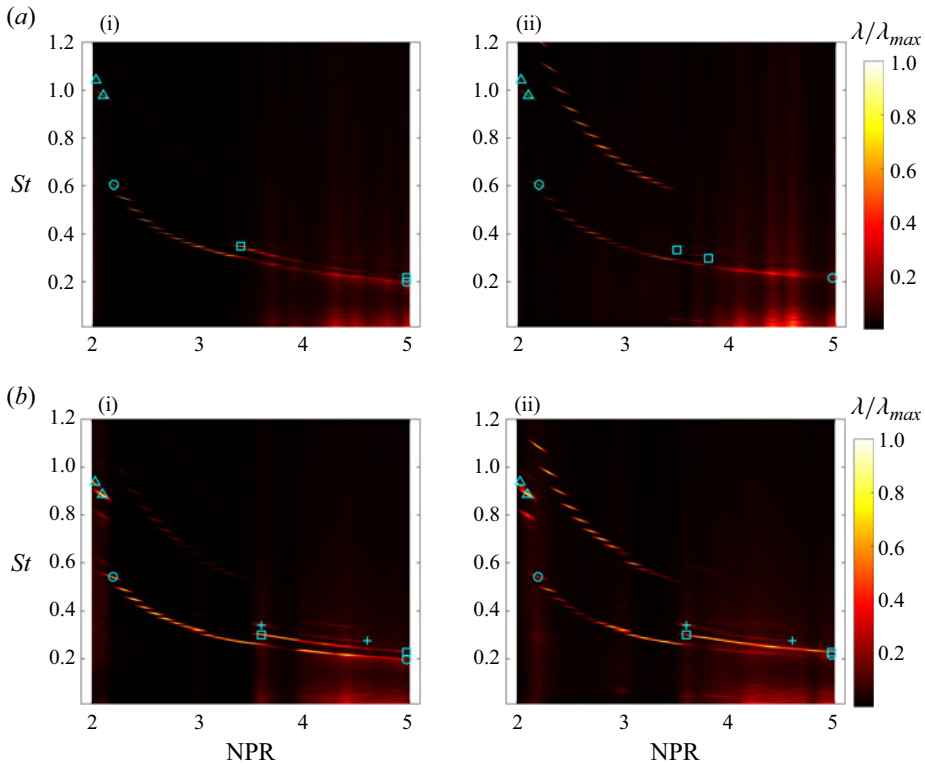
Figure 3. Frequency spectra as a function of nozzle pressure ratio for (*a*) elliptical jet AR $= 2.0$; (*b*) rectangular jet AR $= 2.0$. (*a*-i,*b*-i) $\theta = 0°$. (*a*-ii,*b*-ii) $\theta = 90°$. The cyan triangles (cyan $\triangle$) denote the first peak in the varicose mode. The cyan circles (cyan $\circ$), cyan squares (cyan $\square$) and cyan plus signs (cyan $+$) represent the first (the lowest St_s), second (the middle St_s) and third (the highest St_s) peaks, respectively, identified in the SPOD-eigenvalue spectra shown in figure 2(*c*). To avoid cluttering the figure, only the initial and final pressures at which the peaks appear in the SPOD-eigenvalue spectra are marked.

and major-axis planes. Further, staging behaviour is observed for both jets at NPR $= 2.2$, where screech frequency changes discontinuously. This particular transition represents screech switching from the varicose mode (Tam & Norum 1992) to the flapping mode (Suda *et al.* 1993).

We explore further the varicose and flapping modes using SPOD spatial modes ϕ at screech frequency and associated SPOD eigenvalue λ_s. Figure 4 shows the real part (ϕ_r) and absolute value ($|\phi|$) of SPOD spatial modes for the rectangular jet in the varicose mode at $St_s = 0.92$; each mode here is constructed from a different viewing perspective varying from $\theta = 0°$ to $\theta = 90°$. In this figure, each SPOD spatial mode at each θ is individually normalised using its local maximum such that the maximum value is one. The screech mode is found to be symmetric when viewed from any perspective plane with non-zero amplitude at the centreline and a streamwise peak in the absolute value at $x/D_e \approx 1.4$. As the viewing perspective is moved from the minor-axis plane to the major-axis plane, the projection of the wavepacket covers a larger spanwise extent, suggesting that the initial ring vortex has a non-axisymmetric shape. This finding is aligned with the 3-D structures of wavepackets for non-axisymmetric jets reported by Nogueira *et al.* (2023). Due to the path-integration effect inherent in the schlieren technique, the peak amplitudes of the wavepacket in the cross-wise direction appear at the jet's shear layer in the minor-axis
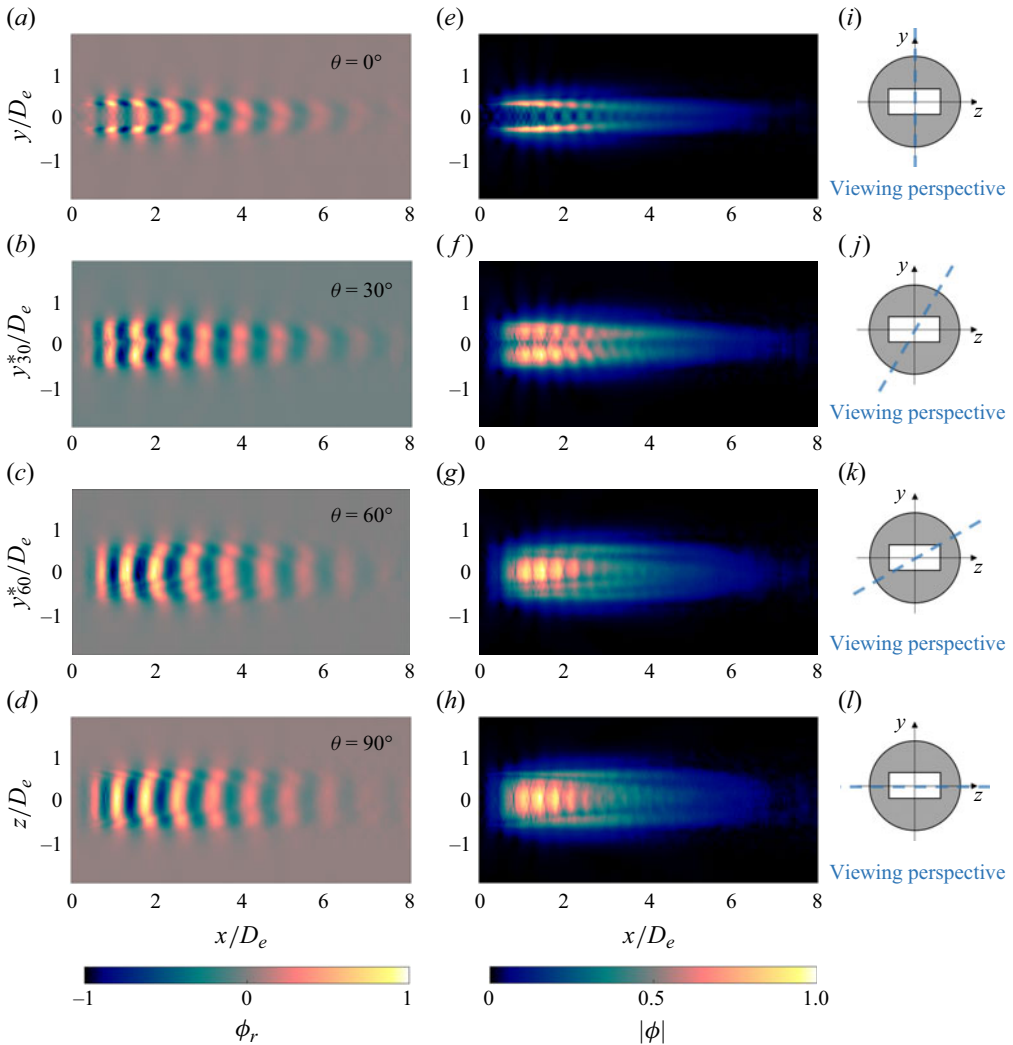
Figure 4. Rectangular jet in varicose mode at $St_s = 0.92$ and NPR = 2.0. (*a–d*) Real part of SPOD spatial mode. (*e–h*) Absolute value of SPOD spatial mode. (*i–l*) Schematic of the viewing perspective.

plane and near the centreline in the major-axis plane. Since the SPOD spatial modes are illustrated only for $\theta = 0°$ to $\theta = 90°$, a normalised inner product, β, is calculated to quantify the agreement between the SPOD spatial modes of supplementary angles. This eliminates the need to display the modes for angles between $\theta = 90°$ and $\theta = 180°$. To demonstrate that the screech mode is symmetrical with respect to the $\theta = 0°$-plane which intersects the z-axis, figure 5(*a*) presents the normalised inner product β, computed using the complex form of SPOD spatial modes obtained when viewed in symmetric planes, i.e. $\theta = 0°$-plane and $\theta = 180°$-plane, $\theta = 10°$-plane and $\theta = 170°$-plane, etc. The complex form of the spatial modes is used to eliminate the effect of any variation in phase between the compared viewing angles.

$$\beta_i = \frac{\langle \phi_{\theta=i}, \phi_{\theta=180°-i} \rangle}{\|\phi_{\theta=i}\| \cdot \|\phi_{\theta=180°-i}\|}, \quad i = 0°, 10°, \ldots, 80°, \tag{3.1}$$
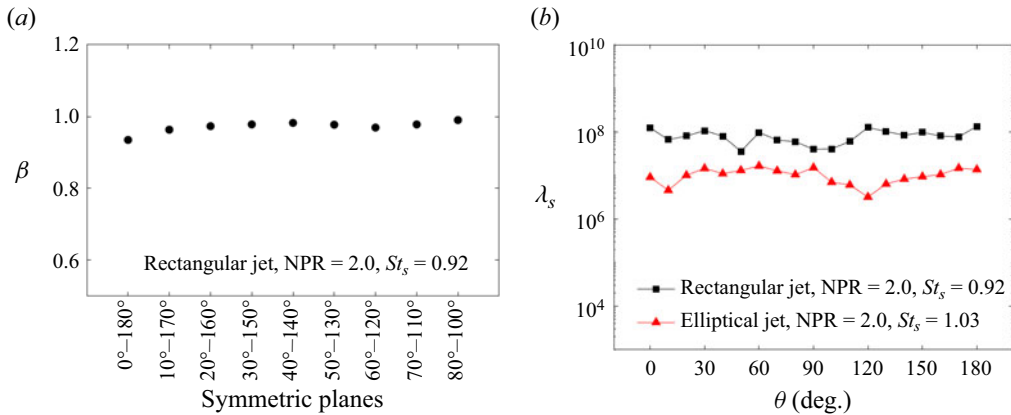
1004 A7-8

Figure 5. (*a*) Cross-correlation coefficient β between symmetric planes around the *z*-axis for a rectangular jet at NPR = 2.0. (*b*) Angular dependence of the SPOD eigenvalue at the screech frequency for both rectangular and elliptical jets in the varicose mode.

where $\langle \cdot , \cdot \rangle$ is the inner product and the double vertical bars denote the Frobenius norm. Here, $\phi_{\theta=i}$ is the SPOD spatial mode at the screech frequency St_s when viewed in the perspective plane $\theta = i^\circ$, whereas $\phi_{\theta=180^\circ-i}$ indicates the SPOD spatial mode at the same frequency in the corresponding symmetrical plane. It should be noted that only the leading mode is used here. The parameter β defined above will range from -1 to 1. The screech mode is considered symmetrical about the *z*-axis when the cross-correlation coefficient β is closest to one, meaning that the SPOD spatial mode viewed in the symmetrical plane $\theta = 180^\circ-i^\circ$ is very similar to what is obtained using $\theta = i^\circ$-plane. Equivalently, $\beta = -1$ represents antisymmetric structures about the *z*-axis, which is not observed in the present case. A β value close to zero indicates uncorrelated screech modes. Figure 5(*a*) shows the computed β of the leading SPOD mode for the rectangular jet operating at NPR = 2.0 and $St_s = 0.92$. It is clear from this figure that symmetric planes produce the same SPOD spatial mode, with coefficients greater than 0.93. Though not shown here for brevity, similar flow behaviour is also observed in the elliptical case.

The varicose mode is further characterised using the SPOD eigenvalue λ_s at the corresponding screech frequency. Evolution of λ_s for both rectangular and elliptical jets are presented in figure 5(*b*) as the viewing perspective is varied from $\theta = 0^\circ$ to $\theta = 180^\circ$. Because the broadband region in the SPOD-eigenvalue spectra is not the same for different θ, a correction is applied to the spectra to isolate the amplitude of the peak itself and discount any changes in the broadband spectrum. This correction ensures that all peaks are referenced to a common baseline. It should be noted that this reference point can be any arbitrary value of λ; for convenience in calculating the correction factor, $\lambda = 0$ has been chosen here. The correction coefficient is calculated based on the local average of non-screech frequency around a fine peak and then subtracting the corresponding local average $\bar{\lambda}$ from the peak value λ_s. This process is performed as to isolate the energy of the screech tone from different perspectives, and it leads to results that are in-line with the expected trends for the dominant modes. It is important to highlight that, even though the correction clarifies some of the trends, the present results are not strongly dependent on the correction process. As shown in figure 5(*b*), the corrected λ_s is found to be relatively constant for different θ, indicating that the fundamental screech frequency is dominant in all axes.
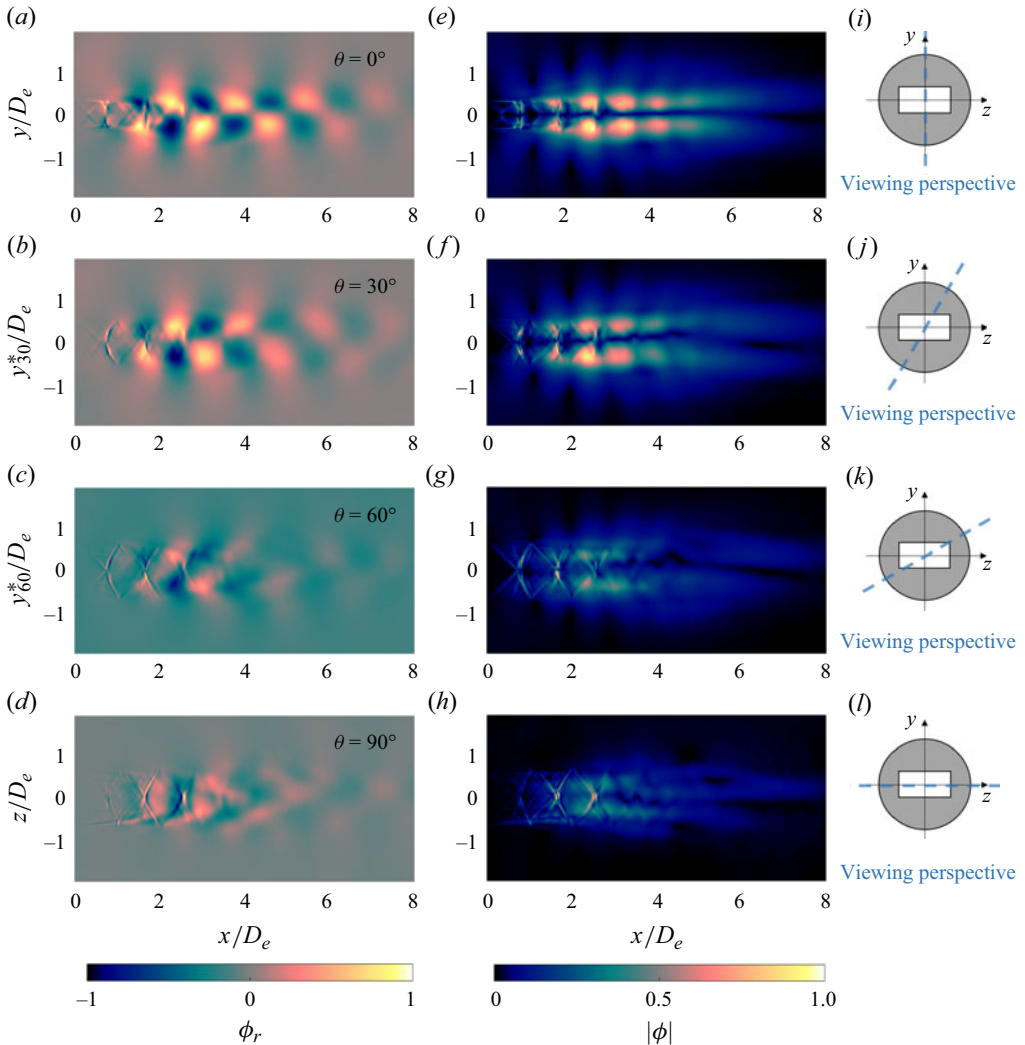
Figure 6. Rectangular jet in flapping mode at $St_s = 0.39$ and NPR = 2.6. (*a–d*) Real part of SPOD spatial mode. (*e–h*) Absolute value of SPOD spatial mode. (*i–l*) Schematic of the viewing perspective.

Figure 6 displays SPOD spatial modes for the rectangular jet operating at NPR = 2.6 and $St_s = 0.39$ as the viewing plane is varied from the minor-axis plane to the major-axis plane. In this figure, each SPOD spatial mode at each θ is again individually normalised using its own local maximum. The real part of the spatial mode observed at $\theta = 0°$ is antisymmetric about the centreline and the absolute value is zero at the centreline; this pattern is consistent with either a helical or flapping motion. If the structures were associated with a helical motion, they would be invariant with respect to the viewing perspective. Here instead, the antisymmetric pattern weakens gradually as θ increases before fully disappearing when viewed in the major-axis plane ($\theta = 90°$). The structure shown for this angle should be interpreted simply as a residual from the path integration, which should cancel most of the flapping behaviour observed for $\theta = 0°$. The amplitude of the mode has a streamwise peak at $x/D_e \approx 2.5$ for all viewing angles. Though not shown
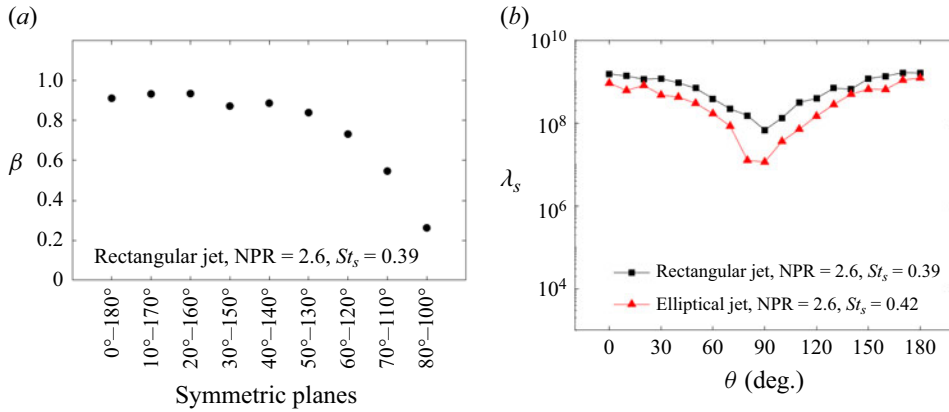
Figure 7. (*a*) Cross-correlation coefficient β between symmetric planes around the z-axis for a rectangular jet at NPR $= 2.6$. (*b*) Angular dependence of the SPOD eigenvalue at the screech frequency for both rectangular and elliptical jets in the flapping mode.

here for brevity, qualitatively similar spatial modes are observed for a flapping elliptical jet.

Like the varicose mode, symmetry of the flapping mode around the z-axis is examined through the cross-correlation coefficient β. The results show a high similarity between SPOD spatial modes produced using planes of $\theta = 0°$ to $\theta = 60°$ and corresponding symmetrical planes of $\theta = 180°$ to $\theta = 120°$ with the β greater than 0.75 (see figure 7*a*). A lower β for planes close to the major-axis plane is attributed to the weak SPOD spatial mode appearing when viewed in those planes; these modes are likely unconverged. Unlike the varicose mode, the SPOD eigenvalue associated with the screech frequency does not remain constant when the viewing perspective is varied from the minor-axis plane to the major-axis plane. As shown in figure 7(*b*), λ_s decreases gradually from $\theta = 0°$ and reaches a minimum at $\theta = 90°$ in the major-axis plane. As the viewing perspective rotates again towards the minor-axis plane, i.e. $\theta = 180°$, the SPOD eigenvalue increases and approaches the value at $\theta = 0°$. This finding is consistent with results in figure 6 indicating that a strong flapping occurs in the minor-axis plane.

4. Bi-axial flapping mode in rectangular jets

The focus of this section is to characterise a new mode observed in the rectangular jet when the multimodal behaviour occurs. This mode, which has been marked by squares ($\square$) in figures 2(*c*) and 3(*b*), exhibits new features that are distinct from those reported for the varicose and flapping modes. The real part and absolute value of SPOD spatial modes for the rectangular jet operating at NPR $= 4.0$ and screech frequency $St_s = 0.27$ are shown in figure 8, as the viewing-perspective angle is varied from $\theta = 0°$ to $\theta = 90°$. Each SPOD spatial mode at each θ is individually normalised using its local maximum. Note that since the wavepacket amplitude envelope extends significantly further downstream for NPR > 3.5, a larger field of view was used compared with that used in § 3. The axial length of the domain size is $12.5D_e$ starting at $x/D_e = 2.5$ from the nozzle lip rather than $x/D_e = 0.0$. Unlike the varicose and flapping modes, a strong antisymmetric pattern about the x-axis (spanwise plane in the 3-D view) is evident from every perspective plane, with zero amplitude at the centreline. The position of the peak wavepacket amplitude is found to vary with the viewing perspective; while the peak in the minor-axis plane is at approximately $x/D_e = 6.5$ and it gradually moves further downstream as θ increases such
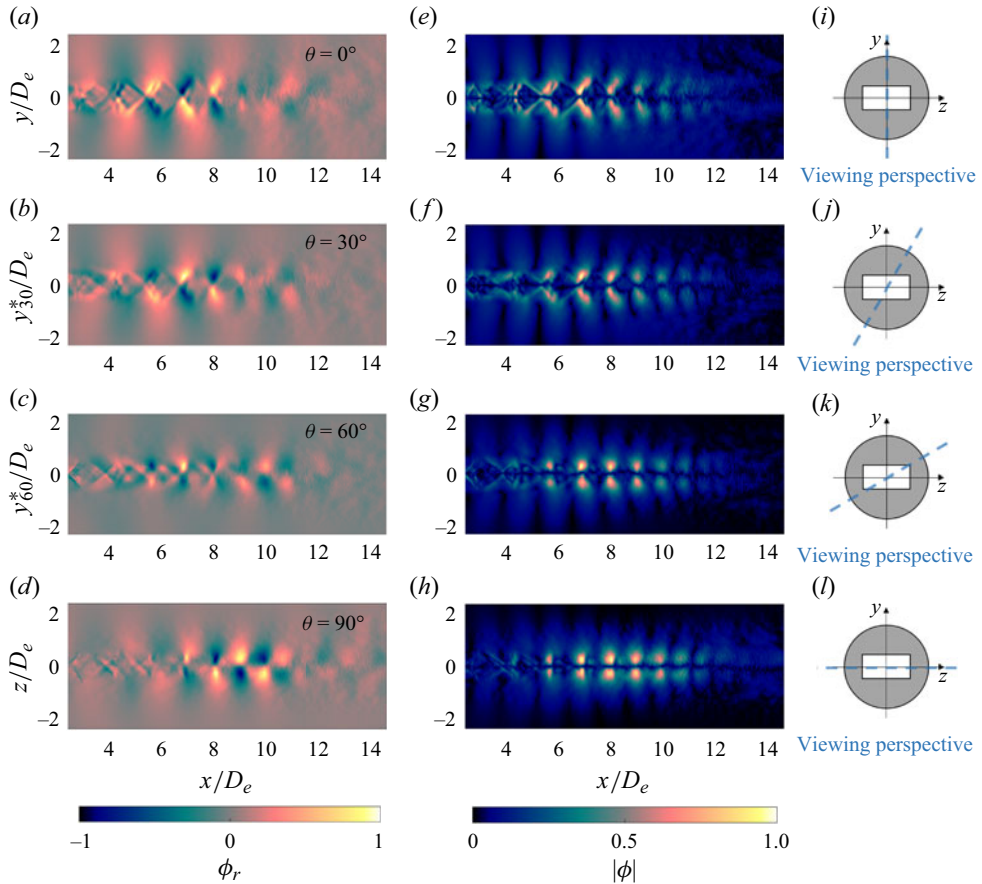
Figure 8. Rectangular jet in bi-axial flapping mode at $St_s = 0.27$ and NPR = 4.0. (*a–d*) Real part of SPOD spatial mode. (*e–h*) Absolute value of SPOD spatial mode. (*i–l*) Schematic of the viewing perspective.

that the peak occurs at $x/D_e = 8.1$ in the major-axis plane. This result is surprising, to say the least; while it is well recognised that the amplitude envelope of wavepackets is a function of frequency (Cavalieri *et al.* 2013; Maia *et al.* 2019), the spatial modes plotted here are all for the same frequency $St_s = 0.27$ and should represent the same coherent structures associated with the screech mode. A wavepacket at a single frequency exhibiting a streamwise shift in its amplitude envelope has not, to our knowledge, been previously reported.

The existence of what appear to be both flapping and wagging modes at a single frequency, with a streamwise-position dependence, suggests a significant axial variation in the mean flow, beyond the typical behaviour observed in axisymmetric jets. One possible mechanism by which a drastic modification of the mean flow might occur is axis switching. In a supersonic jet, axis switching not only modifies the spanwise structure of the shear layer, but by doing so, it also changes the 3-D shape of the shock and expansion cells. These shock structures are relatively straightforward to visualise, providing a means to identify the axis-switching location. The schlieren data are temporally averaged to produce the mean flow $\bar{I}$. Time-averaged visualisations of the density gradient in the streamwise direction ($\partial\rho/\partial x$) are presented in figure 9(*a,b*), individually normalised using local maxima in the minor-axis and major-axis planes, respectively. Bright and dark regions
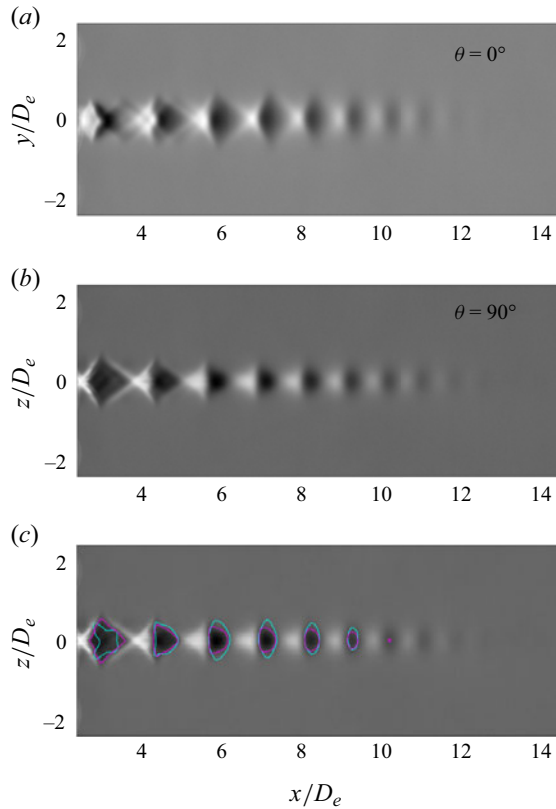
Figure 9. Time-averaged shock structures for the rectangular jet at NPR $= 4.0$ when viewed in (*a*) the minor-axis plane and (*b*) the major-axis plane. (*c*) Comparison of spanwise size of the shock-cell structures; shock cells are marked by cyan and magenta solid lines in the minor-axis plane and major-axis plane, respectively.

indicate the presence of compression and expansion waves, respectively. It should be noted that the first shock cell visible in figure 9 is actually the second shock cell after the nozzle; the first shock cell is located before the beginning of the domain imaged here. The spanwise extent of the shock-cell structure changes as a function of the downstream distance from the nozzle, increasing when viewed from $\theta = 0°$ and decreasing when viewed from $\theta = 90°$. The spanwise extent of the shock cells is used as a crude criterion to indicate the location of axis switching. To qualitatively show variation in the spanwise size of the shock-cell structures, exterior boundaries of the dark regions of the shock cells in the minor and major axes are marked by cyan and magenta colours, respectively, as shown in figure 9(*c*), where they are overlaid on the original image as viewed in the major-axis plane. The exterior boundaries are determined via a boundary-tracing technique applied to binarised versions of figure 9(*a,b*). By this metric, the axes switch at approximately $x/D_e = 6.5$ at approximately the third shock cell in figure 9(*c*), i.e. the fourth shock cell of the jet. At this point, the shock cell in the major-axis plane is clearly smaller than that in the minor-axis plane, in contrast to the state of the flow at the exit from the nozzle.

We now seek to provide further clarity of the nature of the bi-axial mode observed at $St_s = 0.27$, and determine if its behaviour can be correlated with the observed point of axis switching. To this end, the schlieren data are subdivided into smaller streamwise spatial
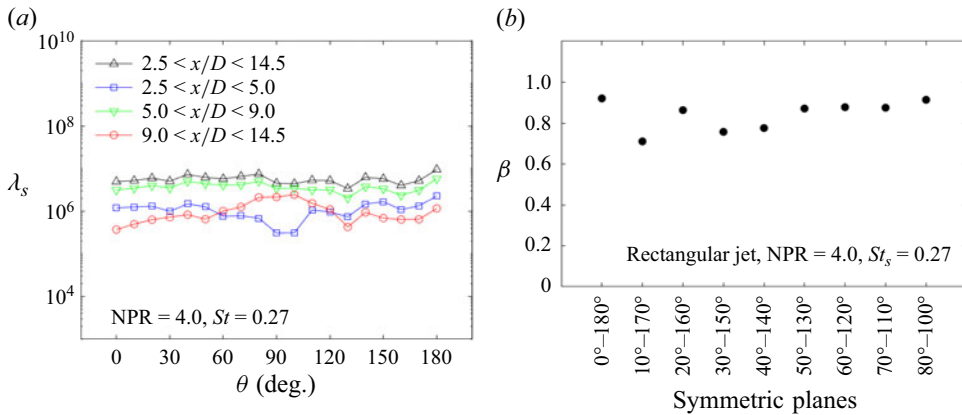
Figure 10. Rectangular jet exhibiting bi-axial mode at $St_s = 0.27$ and NPR $= 4.0$. (*a*) Angular dependence of λ_s for various subdomains. (*b*) Cross-correlation coefficient β between symmetric planes around the z-axis.

domains, and the resultant SPOD-eigenvalues λ_s are compared against the full-domain value. One subdomain covers the axial distance $2.5 < x/D_e < 5.0$, spanning the first three shock cells of the jet, prior to when axis switching occurs. The second subdomain extends over the axial distance $5.0 < x/D_e < 9.0$, spanning the region where axis switching occurs, and the final subdomain covers the range $9.0 < x/D_e < 14.5$, after axis switching has occurred. As shown in figure 10(*a*), λ_s remains nearly constant for any viewing perspective when the whole domain size is considered; the mode represents the same 'energy' of fluctuation irrespective of from which angle it is viewed. An important caveat should be restated here that the SPOD is not based on any intrinsic flow property, but instead is calculated on light intensity fluctuation. The energy being invariant with viewing angle is consistent with a varicose mode, as shown in figure 5, and would also be consistent with a helical $m = 1$ mode. The spatial modes presented in figure 8 rule out a varicose mode, and the streamwise and angle-dependent wavepacket amplitude is inconsistent with a pure helical mode. An angle-dependent eigenvalue amplitude emerges when the subdomains are considered instead. For subdomain $2.5 < x/D_e < 5.0$ (see blue □ in figure 10), the relationship between viewing angle and eigenvalue closely mimics what was observed for a pure flapping mode in figure 7, suggesting the flow here most closely resembles a flapping mode in the minor-axis plane before the axis-switching point. The region that spans the axis-switching location $5.0 < x/D_e < 9.0$ (see green ∇ in figure 10) behaves similarly to the full domain; this region has contributions from the behaviour both upstream and downstream of the axis-switching location. Finally, the subdomain located after the axis-switching location, i.e. $9.0 < x/D_e < 14.5$ (red ○ in figure 10), presents an angular dependence that is $\theta = 90°$ phase shifted from that exhibited by the first subdomain. The most straightforward explanation is that this is a flapping mode in the major-axis plane, which for clarity is typically referred to as a 'wagging' mode. The three subdomains, taken together, suggest that the axis switching represents a sufficient distortion of the original mean-flow profile that the flapping axis also switches. We term this heretofore undiscovered mode a bi-axial flapping mode. To confirm that these structures represent the same resonant frequency, the symmetry of the bi-axial flapping mode around the z-axis is studied using the earlier cross-correlation method. According to figure 10(*b*), symmetric planes lead to reasonably similar SPOD spatial mode, with coefficients greater than 0.75.
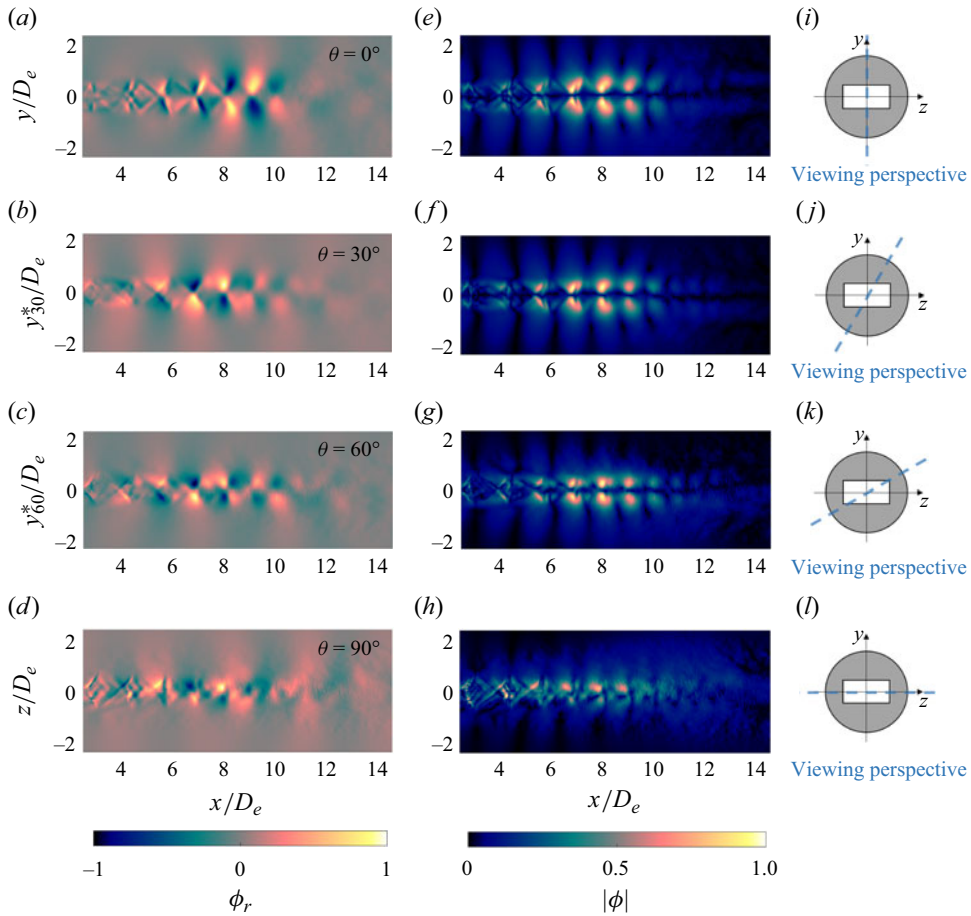
1004 A7-14

Figure 11. Rectangular jet exhibiting flapping mode at $St_s = 0.23$ and NPR = 4.0. (*a–d*) Real part of SPOD spatial mode. (*e–h*) Absolute value of SPOD spatial mode. (*i–l*) Schematic of the viewing perspective.

In addition to the bi-axial flapping mode at screech frequency $St_s = 0.27$, two other screech frequencies $St_s = 0.23$ and 0.30 are also active at NPR = 4.0, as shown in figure 2(*c*). SPOD spatial modes and SPOD eigenvalues λ_s for these screech frequencies are investigated to characterise the two screech modes. SPOD spatial modes at screech frequency $St_s = 0.23$ (marked by circles (○) in figures 2*c* and 3*b*) are qualitatively similar to the pure flapping mode illustrated in figure 6; a clear antisymmetric structure in the minor-axis plane and no coherent structure in the major-axis plane, as shown in figure 11. The variation of λ_s and β with θ shown in figure 12 likewise matches the trends in figure 7; taken together, it is evident that the screech mode at $St_s = 0.23$ is a straightforward flapping mode. Results in figure 12(*a*) reveal that regardless of the axial distance from the nozzle lip, this screech mode consistently flaps in the minor-axis plane, indicating that this mode appears insensitive to axis switching. Furthermore, symmetry of the flapping mode around the z-axis is confirmed by means of β greater than 0.85 for planes $0°$–$180°$ to $60°$–$120°$ (see figure 12*b*). As for NPR = 2.6, the weak signatures in the major-axis plane leave the modes relatively unconverged and, thus, β is small for those planes.

Figure 13 displays the real part and absolute value of SPOD spatial modes for the third screech frequency $St_s = 0.30$, which corresponds to the branch marked by plus
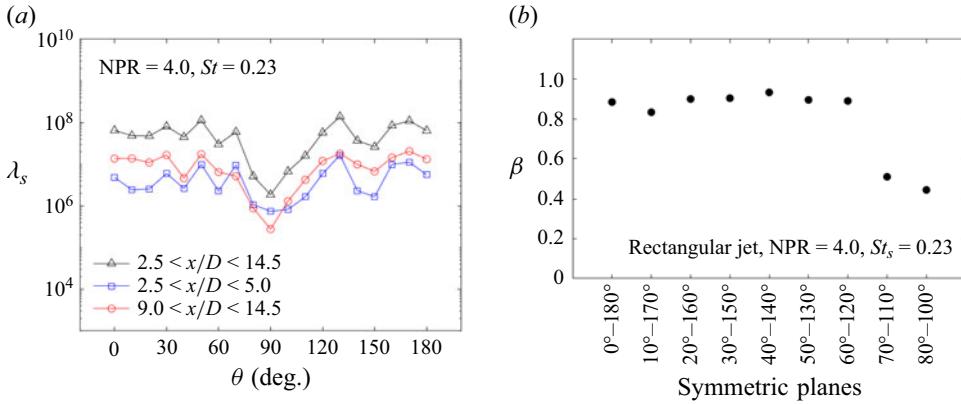
Figure 12. Rectangular jet exhibiting flapping mode at $St_s = 0.23$ and NPR = 4.0. (*a*) Angular dependence of λ_s for various subdomains. (*b*) Cross-correlation coefficient β between symmetric planes around the z-axis.

signs (+) in figures 2(*c*) and 3(*b*). A symmetric pattern is observed when viewed in any perspective plane, indicative of a varicose mode. Both the spatial modes and the relationship of λ_s and θ shown in figure 14(*a*) are reminiscent of those shown in figure 5(*a*), to provide further confirmation of the classification of this mode as varicose. Like the pure flapping screech mode at NPR = 4.0 and $St_s = 0.23$, and unlike the bi-axial flapping mode at NPR = 4.0 and $St_s = 0.27$, this varicose mode does not show any variation in the streamwise location of the peak in wavepacket amplitude with variation in viewing perspective. In addition, $\beta > 0.8$ in figure 14(*b*) demonstrates high similarity between SPOD spatial modes obtained using symmetric planes, confirming the symmetry of screech modes around the z-axis.

5. Quasi-helical mode in elliptical jets

The multimodal behaviour of an elliptical jet is distinctly different from that in a rectangular jet, as demonstrated in figure 3. In this section, we investigate whether the screech modes produced by the elliptical jet when exhibiting multimodality are similarly distinct. As demonstrated in § 3, the behaviour of the elliptical and rectangular jets are similar in the pure flapping and varicose modes. In this multimodal region, we first characterise the screech mode marked by cyan circles (○) in figure 3(*a*) for NPR > 3.5. SPOD spatial modes associated with varying viewing angles for the mode at NPR = 3.6 and $St_s = 0.28$ are shown in figure 15. Like the bi-axial flapping modes, this screech mode is strongly antisymmetric when viewed from any perspective. Given the hypothesised role of axis switching in the bi-axial flapping mode examined previously, we consider how the shock structures of the elliptical jet at this pressure ratio develop in the streamwise direction. The same technique described in § 4 is used here to highlight the spanwise sizes of shock-cell structures. As shown in figure 16, though a complete axis switching does not take place in the domain imaged here, the shock cells in the major-axis plane nonetheless undergo a more rapid contraction with streamwise distance than those in the minor axis. The spanwise extent of the seventh shock cell in the major-axis plane approaches that of the same shock cell in the minor-axis plane, at approximately $x/D_e = 7.5$. This location aligns reasonably well with the peak in the wavepacket amplitude envelope, which occurs at $x/D_e \approx 8$ in figure 15. The initially elliptical profile is undergoing, at the very least,
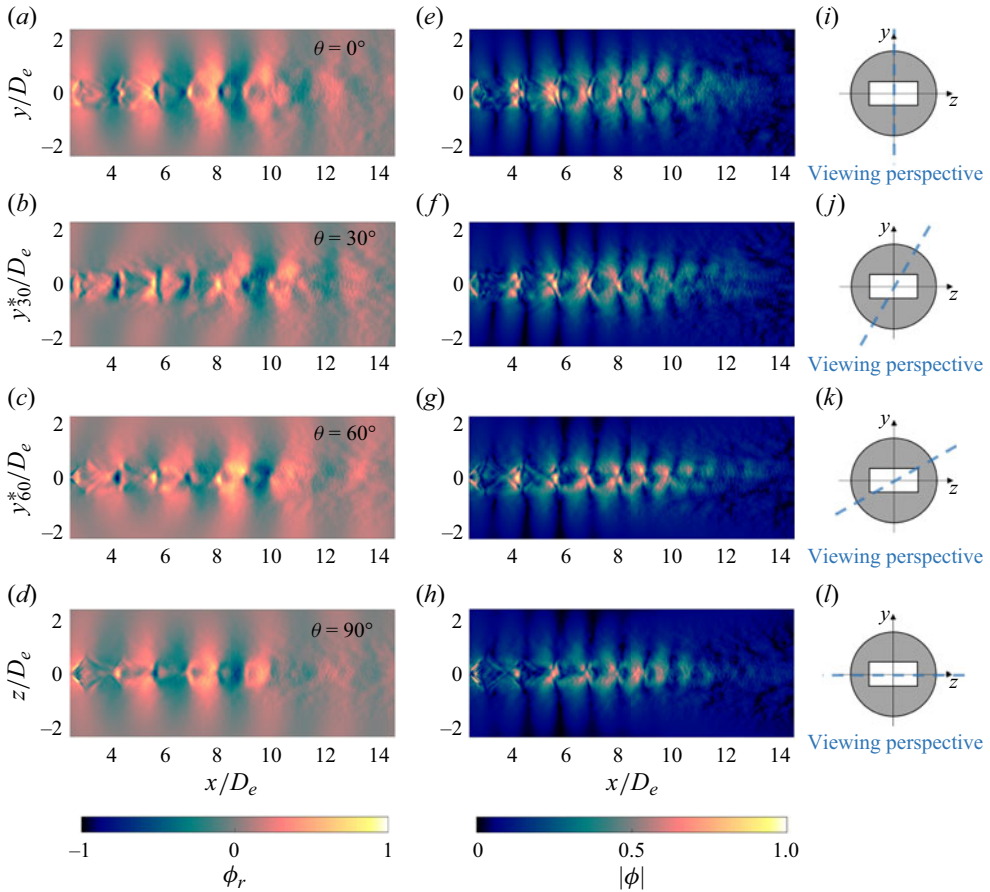
1004 A7-16

Figure 13. Rectangular jet exhibiting varicose mode at $St_s = 0.30$ and NPR = 4.0. (*a–d*) Real part of SPOD spatial mode. (*e–h*) Absolute value of SPOD spatial mode. (*i–l*) Schematic of the viewing perspective.
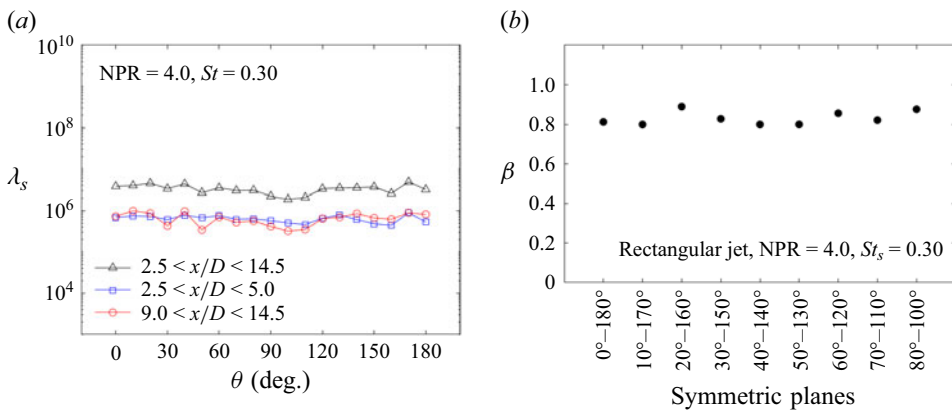

Figure 14. Rectangular jet exhibiting varicose mode at $St_s = 0.30$ and NPR = 4.0. (*a*) Angular dependence of λ_s for various subdomains. (*b*) Cross-correlation coefficient β between symmetric planes around z-axis.
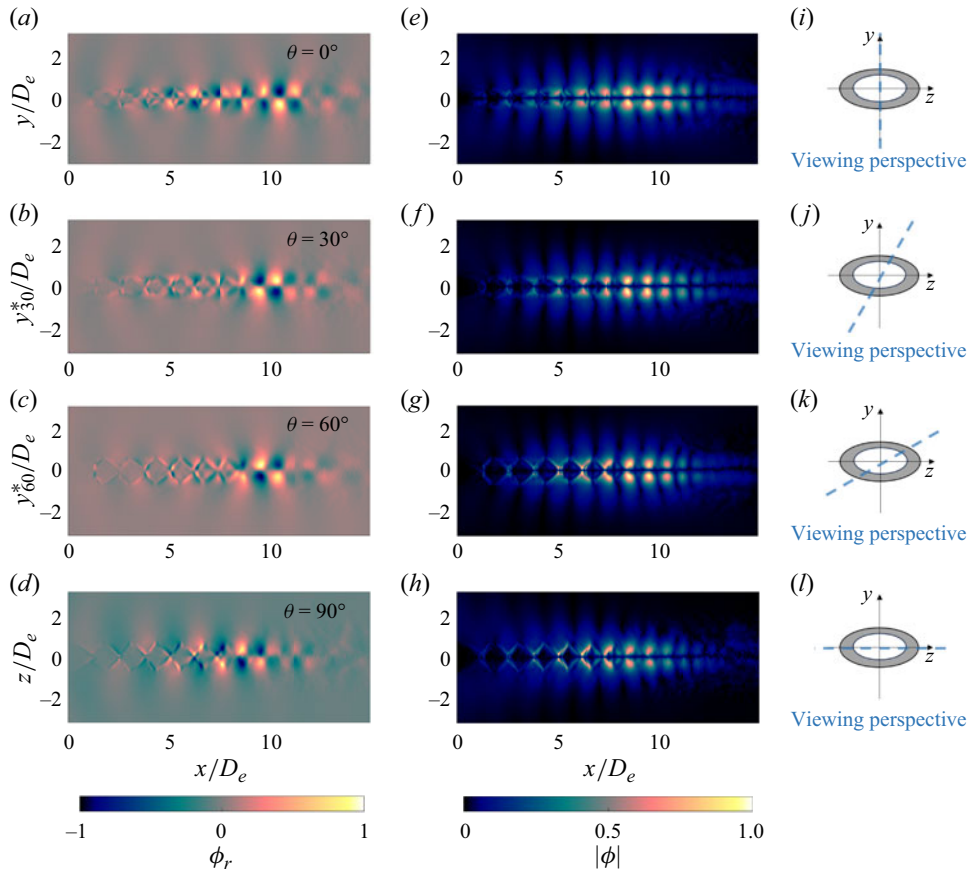
Figure 15. Elliptical jet in the quasi-helical mode at $St_s = 0.28$ and NPR $= 3.6$. (a–d) Real part of SPOD spatial mode. (e–h) Absolute value of SPOD spatial mode. (i–l) Schematic of the viewing perspective.

a reduction in eccentricity, perhaps even a circularisation, with increasing downstream distance.

Global and axial local variations of SPOD eigenvalue λ_s with θ are used to further elucidate the nature of this screech mode. Three subdomains based on axial distance from the nozzle lip are defined to cover an initial region spanning the first two shock cells, i.e. $0.0 < x/D_e < 3.0$, a region spanning the axis-switching location ($3.0 < x/D_e < 11.0$) and a section well downstream of the axis switch, i.e. $11.0 < x/D_e < 14.5$. As shown in figure 17(a), λ_s is found to be reasonably constant at approximately 10^7 for all angles when considering the entire domain. All subdomains evidence similar behaviour, with reduced amplitude for the small domains but the same relationship with angle. The insensitivity of λ_s to viewing angle and subdomain suggests that this mode is not exhibiting a bi-axial flapping. Given the antisymmetry of the structures in the SPOD spatial modes when viewed from any viewing perspective, and the lack of streamwise variation, we suggest that this mode most closely resembles a helical mode, as observed in axisymmetric jets. As the mean flow is not axisymmetric, and thus is difficult to effectively decompose on an azimuthal basis, we stop short of calling this mode helical, but instead adopt the label 'quasi-helical'. Further characterisation of the quasi-helical mode, including helicity measurements, requires velocity data from the jet cross-section, which is beyond the scope
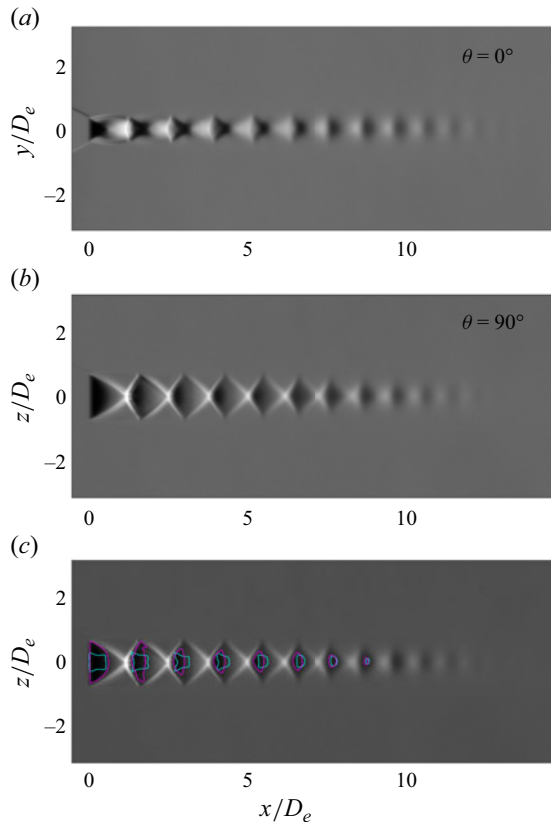
1004 A7-18

Figure 16. Time-averaged shock structures for the elliptical jet at NPR = 3.6 when viewed in (*a*) the minor-axis plane and (*b*) the major-axis plane. (*c*) Comparison of spanwise size of the shock-cell structures; shock cells are marked by cyan and magenta solid lines in the minor-axis plane and major-axis plane, respectively.

of this study. It is worth noting that symmetry of the SPOD spatial modes around the *z*-axis is confirmed by means of $\beta > 0.8$ (see figure 17*b*).

The other screech frequency active at NPR = 3.6 and marked by ($\square$) in figure 3(*a*) is considered last. Figure 18 displays SPOD spatial modes for $St_s = 0.32$ for different viewing planes. Strong antisymmetric patterns in the minor-axis plane accompanied by no clear pattern in the major-axis plane is indicative of a flapping instability in the minor axis. This is reinforced by the variations of λ_s with increasing θ; figure 19(*a*) shows that λ_s depends on θ in the same way as the two flapping modes observed previously in figures 7 and 12. According to figure 19(*a*), this v-shape pattern for λ_s is independent of the axial distance from the nozzle lip, indicating that the screech mode consistently flaps in the minor axis. Furthermore, SPOD spatial modes are found to be symmetrical around the *z*-axis with β greater than 0.7 for symmetric planes $0°$–$180°$ to $60°$–$120°$. Thus, this mode appears to be a classical se_1 flapping mode.

6. Conclusions

The features of two previously unrecognised screech modes in non-axisymmetric jets have been identified for the first time in this study. By analysing ultra-high-speed schlieren
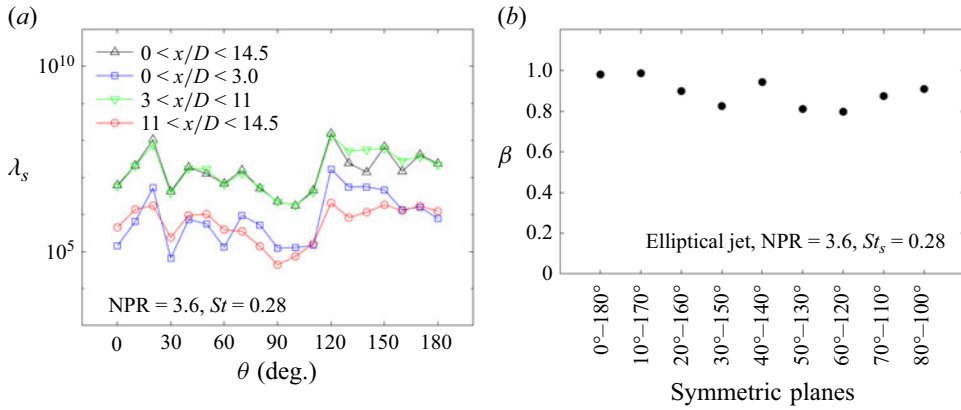
Figure 17. Elliptical jet exhibiting quasi-helical mode at $St_s = 0.28$ and NPR $= 3.6$. (*a*) Angular dependence of λ_s for various subdomains. (*b*) Cross-correlation coefficient β between symmetric planes around the *z*-axis.
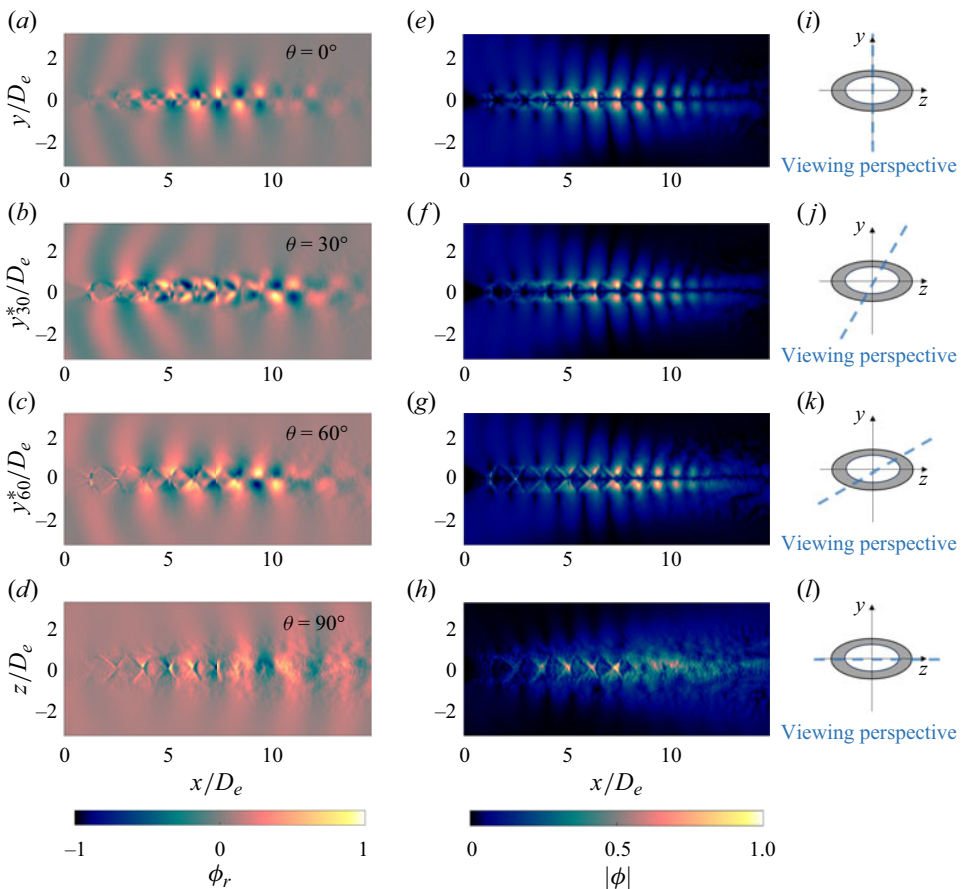

Figure 18. Elliptical jet exhibiting flapping mode at $St_s = 0.32$ and NPR $= 3.6$. (*a*–*d*) Real part of SPOD spatial mode. (*e*–*h*) Absolute value of SPOD spatial mode. (*i*–*j*) Schematic of the viewing perspective.
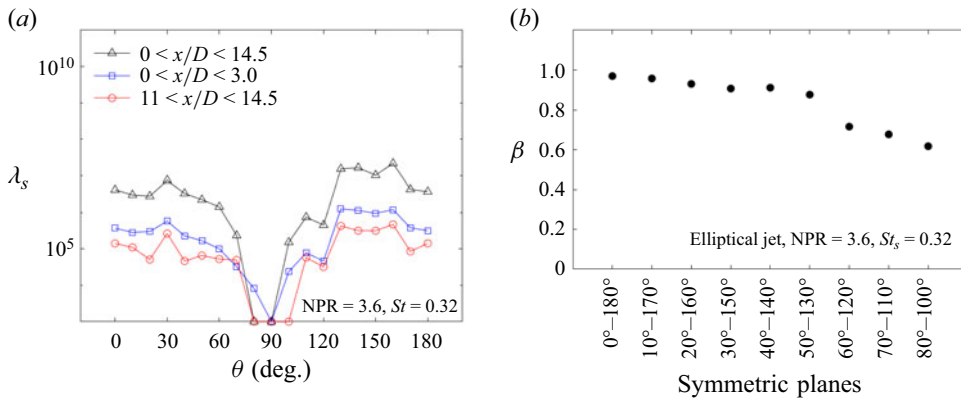
Figure 19. Elliptical jet exhibiting flapping mode at $St_s = 0.32$ and NPR = 3.6. (*a*) Angular dependence of λ_s for various subdomains. (*b*) Cross-correlation coefficient β between symmetric planes around the z-axis.

images using spectral proper orthogonal decomposition (SPOD), a bi-axial flapping mode in a rectangular jet and a quasi-helical mode in an elliptical jet have been discovered. In this study, schlieren measurements have been taken from different azimuthal angles (θ) to reconstruct 3-D flow structures of the supersonic jet.

The bi-axial flapping mode is found to be strongly antisymmetric about the x-axis when viewed from any perspective, but the SPOD eigenvalue at the screech frequency (λ_s) is found to vary depending on θ and the axial distance of the SPOD domain from the nozzle lip. For the region close to nozzle lip, λ_s decreases gradually as the viewing perspective is varied from the minor-axis plane ($\theta = 0°$) to the major-axis plane ($\theta = 90°$), reaching a minimum at $\theta = 90°$. This dependence on angle indicates a flapping mode in the minor-axis plane. In contrast, for a SPOD domain defined further downstream, a gradual increase in λ_s from $\theta = 0°$ to $\theta = 90°$ indicates that in this region, the jet is 'wagging' in the major-axis plane. Taken together, this suggests that the screech mode experiences a transition from a flapping mode to a wagging mode at the same frequency. It is demonstrated that the location at which this switch takes place correlates with the location of axis switching as defined by a consideration of the shock-cell structure in the mean flow.

The quasi-helical mode in the elliptical jet is examined through the same methodology. Distinct from the bi-axial mode in the rectangular jet, this mode is characterised by the antisymmetric structure in the SPOD spatial modes, with an eigenvalue λ_s that remains unaffected by both θ and the axial domain. The discovery of these new structures indicates that in addition to the commonly known screech modes supported by the original 3-D shape of the jet, the axial variation in the mean flow in non-axisymmetric jets could support a variety of additional screech modes.

Declaration of interests. The authors report no conflict of interest.

Author ORCIDs.

- Soudeh Mazharmanesh https://orcid.org/0000-0002-3263-760X;
- Petrônio A.S. Nogueira https://orcid.org/0000-0001-7831-8121;
- Joel Weightman https://orcid.org/0000-0002-6886-3393;
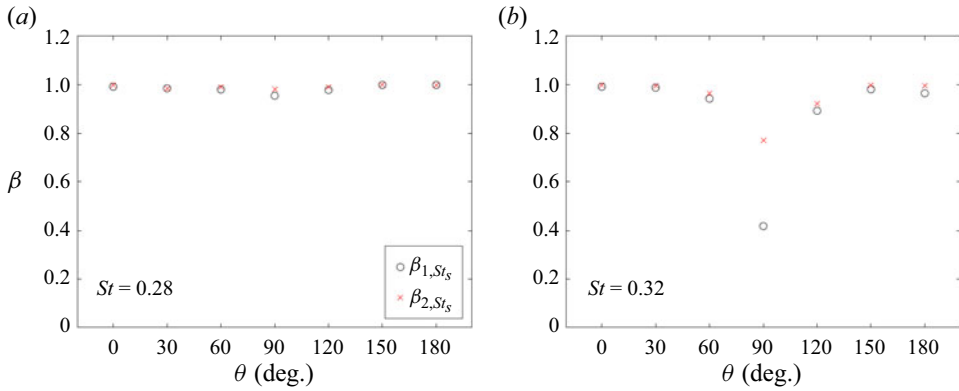- Daniel Edgington-Mitchell https://orcid.org/0000-0001-9032-492X.

Figure 20. Convergence of the SPOD spatial modes for elliptical jet operating at NPR = 3.6 and (a) $St_s = 0.28$ (b) $St_s = 0.32$.

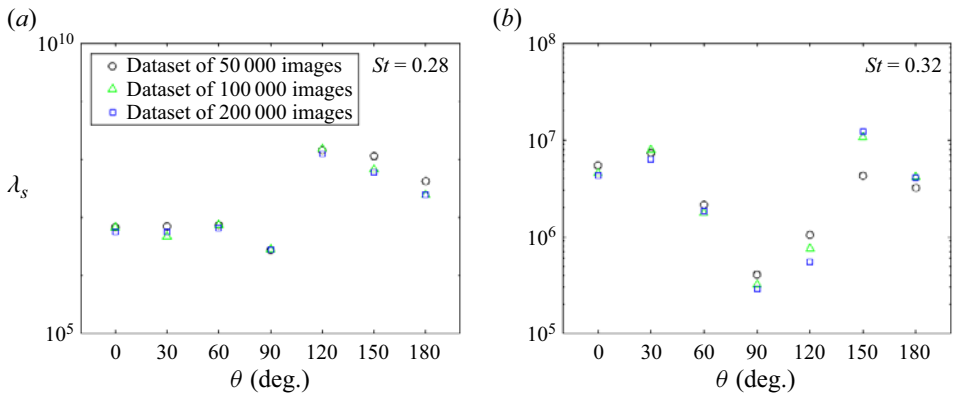Figure 21. Convergence of the SPOD eigenvalue λ_s for elliptical jet operating at NPR = 3.6 and (a) $St_s = 0.28$ (b) $St_s = 0.32$.

Appendix A. Statistical convergence of SPOD modes

The convergence of the computed SPOD modes is analysed by considering three datasets of 50 000, 100 000 and 200 000 images, and performing SPOD on each dataset. A normalised inner product β_{i,St_s} is computed between each SPOD spatial mode ϕ_{i,St_s}, obtained with datasets of 50 000 and 100 000 images, and the corresponding mode ϕ_{St_s}, obtained with the dataset of 200 000 images,

$$\beta_{i,St_s} = \frac{\langle \phi_{St_s}, \phi_{i,St_s} \rangle}{\|\phi_{St_s}\| \cdot \|\phi_{i,St_s}\|}, \tag{A1}$$

where $\langle \cdot, \cdot \rangle$ is the inner product and the double vertical bars denote the Frobenius norm. Also, $i = 1$ and 2 refers to the dataset of 50 000 and 100 000 images, respectively. The SPOD spatial mode is considered as a converged mode when β_{i,St_s} is closest to one. Figure 20 shows the β calculated using the leading modes at screech frequencies $St_s = 0.28$ and 0.32 in the elliptical jet operating at NPR = 3.6. The SPOD mode is found to be converged using the dataset of $i = 2$ with β greater than 0.95 and 0.8 for $St_s = 0.28$ and 0.32, respectively. It should be noted that the SPOD spatial mode at $St_s = 0.32$ and

1004 A7-22

$\theta = 90°$ is very weak, thus $\beta = 0.8$ is ample to have converged SPOD in this particular configuration.

We also examined the sensitivity of the SPOD eigenvalue at screech frequency λ_s to the sample length. As shown in figure 21, the variation of λ_s is less than 6 % when the sample length increases from 100 000 images to 200 000 images. Thus, the dataset of 100 000 images is used in this study. Though not shown here for brevity, similar results are obtained for the rectangular jet.

REFERENCES

ABREU, L.I., TANARRO, A., CAVALIERI, A.V.G., SCHLATTER, P., VINUESA, R., HANIFI, A. & HENNINGSON, D.S. 2021 Spanwise-coherent hydrodynamic waves around flat plates and airfoils. *J. Fluid Mech.* **927**, A1.

BERLAND, J., BOGEY, C. & BAILLY, C. 2007 Numerical study of screech generation in a planar supersonic jet. *Phys. Fluids* **19** (7), 075105.

BOGEY, C. 2021 Acoustic tones in the near-nozzle region of jets: characteristics and variations between Mach numbers 0.5 and 2. *J. Fluid Mech.* **921**, A3.

BOGEY, C. & GOJON, R. 2017 Feedback loop and upwind-propagating waves in ideally expanded supersonic impinging round jets. *J. Fluid Mech.* **823**, 562–591.

CAIN, A., BOWER, W., WALKER, S. & LOCKWOOD, M. 1995 Modeling supersonic jet screech. I-vortical instability wave modeling. In *33rd Aerospace Sciences Meeting and Exhibit, 9–12 January, Reno, NV, USA*, p. 506. AIAA.

CAVALIERI, A.V.G., JORDAN, P. & LESSHAFFT, L. 2019 Wave-packet models for jet dynamics and sound radiation. *Appl. Mech. Rev.* **71** (2), 020802.

CAVALIERI, A.V.G., RODRÍGUEZ, D., JORDAN, P., COLONIUS, T. & GERVAIS, Y. 2013 Wavepackets in the velocity field of turbulent jets. *J. Fluid Mech.* **730**, 559–592.

CHAKRABARTI, S., GAITONDE, D. & UNNIKRISHNAN, S. 2021 Representing rectangular jet dynamics through azimuthal fourier modes. *Phys. Rev. Fluids* **6** (7), 074605.

CRIGHTON, D.G. 1973 Instability of an elliptic jet. *J. Fluid Mech.* **59** (4), 665–672.

DAVIES, M.G. & OLDFIELD, D.E.S. 1962 Tones from a choked axisymmetric jet. I. Cell structure, eddy velocity and source locations. *Acta Acust. United Acust.* **12** (4), 257–267.

EDGINGTON-MITCHELL, D. 2019 Aeroacoustic resonance and self-excitation in screeching and impinging supersonic jets – a review. *Intl J. Aeroacoust.* **18**, 118–188.

EDGINGTON-MITCHELL, D., HONNERY, D.R. & SORIA, J. 2015*a* Multimodal instability in the weakly underexpanded elliptic jet. *AIAA J.* **53** (9), 2739–2749.

EDGINGTON-MITCHELL, D., HONNERY, D.R. & SORIA, J. 2015*b* Staging behaviour in screeching elliptical jets. *Intl J. Aeroacoust.* **14** (7), 1005–1024.

EDGINGTON-MITCHELL, D., JAUNET, V., JORDAN, P., TOWNE, A., SORIA, J. & HONNERY, D. 2018 Upstream-travelling acoustic jet modes as a closure mechanism for screech. *J. Fluid Mech.* **855**, R1.

EDGINGTON-MITCHELL, D., LI, X., LIU, N., HE, F., WONG, T.Y., MACKENZIE, J. & NOGUEIRA, P. 2022*a* A unifying theory of jet screech. *J. Fluid Mech.* **945**, A8.

EDGINGTON-MITCHELL, D.M., BEEKMAN, J. & NOGUEIRA, P. 2022*b* Screech mode staging in rectangular and elliptical jets. In *28th AIAA/CEAS Aeroacoustics 2022 Conference, 14–17 June, Southampton, UK*, p. 3023. AIAA.

GAO, J.H. & LI, X.D. 2010 A multi-mode screech frequency prediction formula for circular supersonic jets. *J. Acoust. Soc. Am.* **127** (3), 1251–1257.

GOJON, R., BOGEY, C. & MIHAESCU, M. 2018 Oscillation modes in screeching jets. *AIAA J.* **56** (7), 2918–2924.

GUTMARK, E., SCHADOW, K.C. & WILSON, K.J. 1989 Noncircular jet dynamics in supersonic combustion. *J. Propul. Power* **5** (5), 529–533.

GUTMARK, E.J. & GRINSTEIN, F.F. 1999 Flow control with noncircular jets. *Annu. Rev. Fluid Mech.* **31** (1), 239–272.

HARPER-BOURNE, M. & FISHER, M. 1974 The noise from shock waves in supersonic jets. *AGARD Tech. Rep.* CP 131.

HO, C.-M. & GUTMARK, E. 1987 Vortex induction and mass entrainment in a small-aspect-ratio elliptic jet. *J. Fluid Mech.* **179**, 383–405.

HUSSAIN, F. & HUSAIN, H.S. 1989 Elliptic jets. Part 1. Characteristics of unexcited and excited jets. *J. Fluid Mech.* **208**, 257–320.

JORDAN, P. & COLONIUS, T. 2013 Wave packets and turbulent jet noise. *Annu. Rev. Fluid Mech.* **45**, 173–195.

KARNAM, A., BAIER, F. & GUTMARK, E.J. 2019 Near field acoustic analysis of cold supersonic rectangular jets. In *AIAA Scitech 2019 Forum, 7–11 January, San Diego, CA, USA*, p. 0809. AIAA.

KARNAM, A., SALEEM, M. & GUTMARK, E. 2023 Influence of nozzle geometry on screech instability closure. *Phys. Fluids* **35** (8), 086119.

KINZIE, K.W. & MCLAUGHLIN, D.K. 1997 Azimuthal mode measurements of elliptic jets. *Phys. Fluids* **9** (7), 2000–2008.

LEE, S.-J. & BAEK, S.-J. 1994 The effect of aspect ratio on the near-field turbulent structure of elliptic jets. *Flow Meas. Instrum.* **5** (3), 170–180.

LEETE, K.M., WALL, A.T., GEE, K.L., NEILSEN, T.B., JAMES, M.M. & DOWNING, J.M. 2021 Acoustical holography-based analysis of spatiospectral lobes in high-performance aircraft jet noise. *AIAA J.* **59** (10), 4166–4178.

LIANG, L.-L., WAN, Z.-H., YE, C.-C., ZHANG, P.-J.-Y., SUN, D.-J. & LU, X.-Y. 2023 Flow dynamics and noise generation mechanisms in supersonic underexpanded rectangular and planar jets. *AIP Adv.* **13** (6), 065128.

LUMLEY, J.L. 1970 *Stochastic Tools in Turbulence*. Academic Press.

MAIA, I.A., JORDAN, P., CAVALIERI, A.V.G., JAUNET, V. 2019 Two-point wavepacket modelling of jet noise. *Proc. R. Soc.* A **475** (2227), 20190199.

MAZHARMANESH, S., NOGUEIRA, P.A.S., WEIGHTMAN, J., BEEKMAN, J.R. & EDGINGTON-MITCHELL, D.M. 2024 Multimodal behaviour in screeching elliptical and rectangular jets. In *30th AIAA/CEAS Aeroacoustics Conference (2024), 4–7 June, Rome, Italy*, p. 3143. AIAA.

MENON, N. & SKEWS, B.W. 2010 Shock wave configurations and flow structures in non-axisymmetric underexpanded sonic jets. *Shock Waves* **20**, 175–190.

MORRIS, P.J. 1988 Instability of elliptic jets. *AIAA J.* **26** (2), 172–178.

MORRIS, P.J. 2010 The instability of high speed jets. *Intl J. Aeroacoust.* **9** (1–2), 1–50.

MORRIS, P.J. & BHAT, T.R.S. 1995 The spatial stability of compressible elliptic jets. *Phys. Fluids* **7** (1), 185–194.

NOGUEIRA, P.A., WEIGHTMAN, J. & EDGINGTON-MITCHELL, D.M. 2023 Prediction of wavepackets in elliptical jets using 3D one-way Navier–Stokes equations. In *AIAA AVIATION 2023 Forum*, p. 3511.

NOGUEIRA, P.A.S., JAUNET, V., MANCINELLI, M., JORDAN, P. & EDGINGTON-MITCHELL, D. 2022*a* Closure mechanism of the A1 and A2 modes in jet screech. *J. Fluid Mech.* **936**, A10.

NOGUEIRA, P.A.S., JORDAN, P., JAUNET, V., CAVALIERI, A.V.G., TOWNE, A. & EDGINGTON-MITCHELL, D. 2022*b* Absolute instability in shock-containing jets. *J. Fluid Mech.* **930**, A10.

NOGUEIRA, P.A.S., SELF, H.W.A., TOWNE, A. & EDGINGTON-MITCHELL, D. 2022*c* Wave-packet modulation in shock-containing jets. *Phys. Rev. Fluids* **7** (7), 074608.

POWELL, A. 1953 On the mechanism of choked jet noise. *Proc. Phys. Soc.* B **66** (12), 1039.

POWELL, A., UMEDA, Y. & ISHII, R. 1992 Observations of the oscillation modes of choked circular jets. *J. Acoust. Soc. Am.* **92** (5), 2823–2836.

RAJAKUPERAN, E. & RAMASWAMY, M.A. 1998 An experimental investigation of underexpanded jets from oval sonic nozzles. *Exp. Fluids* **24** (4), 291–299.

RAMAN, G. 1997 Screech tones from rectangular jets with spanwise oblique shock-cell structures. *J. Fluid Mech.* **330**, 141–168.

RAMAN, G. & RICE, E.J. 1994 Instability modes excited by natural screech tones in a supersonic rectangular jet. *Phys. Fluids* **6** (12), 3999–4008.

SANO, A., ABREU, L.I., CAVALIERI, A.V.G. & WOLF, W.R. 2019 Trailing-edge noise from the scattering of spanwise-coherent structures. *Phys. Rev. Fluids* **4** (9), 094602.

SCHMIDT, O.T. & COLONIUS, T. 2020 Guide to spectral proper orthogonal decomposition. *AIAA J.* **58** (3), 1023–1033.

SCHMIDT, O.T., TOWNE, A., COLONIUS, T., CAVALIERI, A.V.G., JORDAN, P. & BRÈS, G.A. 2017 Wavepackets and trapped acoustic modes in a turbulent jet: coherent structure eduction and global stability. *J. Fluid Mech.* **825**, 1153–1181.

SCHMIDT, O.T., TOWNE, A., RIGAS, G., COLONIUS, T. & BRES, G.A. 2018 Spectral analysis of jet turbulence. *J. Fluid Mech.* **855**, 953–982.

SEMLITSCH, B., MALLA, B., GUTMARK, E.J. & MIHĂESCU, M. 2020 The generation mechanism of higher screech tone harmonics in supersonic jets. *J. Fluid Mech.* **893**, A9.

SINGH, A. & CHATTERJEE, A. 2007 Numerical prediction of supersonic jet screech frequency. *Shock Waves* **17**, 263–272.

SUDA, H., MANNING, T. & KAJI, S. 1993 Transition of oscillation modes of rectangular supersonic jet in screech. In *15th Aeroacoustics Conference, 25–27 October, Long Beach, CA, USA*, p. 4323. AIAA.

SUZUKI, N., NOGUEIRA, P. & EDGINGTON-MITCHELL, D. 2023 Analysis of elliptical-jet acoustic directivity and efficiency using a vortex-sheet-based wave-packet model. *AIAA J.* **61** (6), 2570–2580.

TAM, C.K.W. 1995 Supersonic jet noise. *Annu. Rev. Fluid Mech.* **27** (1), 17–43.

TAM, C.K.W. & AHUJA, K.K. 1990 Theoretical model of discrete tone generation by impinging jets. *J. Fluid Mech.* **214**, 67–87.

TAM, C.K.W. & HU, F.Q. 1989 On the three families of instability waves of high-speed jets. *J. Fluid Mech.* **201**, 447–483.

TAM, C.K.W. & NORUM, T.D. 1992 Impingement tones of large aspect ratio supersonic rectangular jets. *AIAA J.* **30** (2), 304–311.

TAM, C.K.W. & TANNA, H.K. 1982 Shock associated noise of supersonic jets from convergent-divergent nozzles. *J. Sound Vib.* **81** (3), 337–358.

TOWNE, A., CAVALIERI, A.V.G., JORDAN, P., COLONIUS, T., SCHMIDT, O., JAUNET, V. & BRÈS, G.A. 2017 Acoustic resonance in the potential core of subsonic jets. *J. Fluid Mech.* **825**, 1113–1152.

TOWNE, A., SCHMIDT, O.T. & COLONIUS, T. 2018 Spectral proper orthogonal decomposition and its relationship to dynamic mode decomposition and resolvent analysis. *J. Fluid Mech.* **847**, 821–867.

UMEDA, Y., ISHII, R., MATSUDA, T., YASUDA, A., SAWADA, K. & SHIMA, E. 1990 Instability of astrophysical jets. II. Numerical simulation of two-dimensional choked underexpanded slab jets. *Prog. Theor. Phys.* **84** (5), 856–866.

VISWANATH, K., JOHNSON, R., CORRIGAN, A., KAILASANATH, K., MORA, P., BAIER, F. & GUTMARK, E. 2017 Flow statistics and noise of ideally expanded supersonic rectangular and circular jets. *AIAA J.* **55** (10), 3425–3439.

WELCH, P. 1967 The use of fast fourier transform for the estimation of power spectra: a method based on time averaging over short, modified periodograms. *IEEE Trans. Audio Electroacoust.* **15** (2), 70–73.

WILLERT, C., STASICKI, B., KLINNER, J. & MOESSNER, S. 2010 Pulsed operation of high-power light emitting diodes for imaging flow velocimetry. *Meas. Sci. Technol.* **21** (7), 075402.

WLEZIEN, R.W. & KIBENS, V. 1988 Influence of nozzle asymmetry on supersonic jets. *AIAA J.* **26** (1), 27–33.

WONG, T.Y.M., STAVROPOULOS, M.N., BEEKMAN, J.R., TOWNE, A., NOGUEIRA, P.A.S., WEIGHTMAN, J. & EDGINGTON-MITCHELL, D. 2023 Steady and unsteady coupling in twin weakly underexpanded round jets. *J. Fluid Mech.* **964**, A2.

YOON, J.-H. & LEE, S.-J. 2003 Investigation of the near-field structure of an elliptic jet using stereoscopic particle image velocimetry. *Meas. Sci. Technol.* **14** (12), 2034.